Supporting Information

Visualizing and controlling of photogenerated electron-hole pair separation in monolayer WS_2 nanobubbles under piezoelectric field

Sheng Han[1,#], Jiong Liu[1,#], Ana I. Pérez-Jiménez[3], Zhou Lei[1], Pei Yan[1], Yu Zhang[1], Xiangyu Guo[1], Rongxu Bai[1], Shen Hu[1,5,*], Xuefeng Wu[1,2,*], David W. Zhang[1,2,5,6], Qingqing Sun[1,2,5], Deji Akinwande[4], Edward T. Yu[4,*], Li Ji[1,2,5,6,*]

[1]School of Microelectronics, Fudan University, Shanghai 200433, China.

[2]Shanghai Integrated Circuit Manufacturing Innovation Center, Shanghai 201210, China.

[3]Technology Innovation Institute, 9639, Masdar City, Abu Dhabi, United Arab Emirates

[4]Microelectronic Research Center, Department of Electrical and Computer Engineering, The University of Texas at Austin, Austin 78758, United States.

[5]Jiashan Fudan Institute, Jiaxing 314110, China.

[6]Hubei Yangtze Memory Laboratories, Wuhan 430205, China.

[#] *These authors contributed equally to this work.*

*Corresponding to: hushen@fudan.edu.cn; xuefeng.wu@shnicic.com; ety@ece.utexas.edu; lji@fudan.edu.cn;

Methods

Sample preparation. Samples were prepared using the standard dry transfer technique. Monolayer WS_2 and monolayer graphene was mechanically exfoliated with Polydimethylsiloxane (PDMS). The parent materials of the membrane were then transferred and stacked to the Si/SiO_2 substrate with a series of delicate micro-operations based on a set of micromanipulation stages. The PDMS was taken away by easily peeling back the membrane. This process ensured the cleanliness of two-dimensional crystal surface w/o the introduction of any solution.

AFM and KPFM experiments were acquired in a HORIBA Smart SPM. AFM height images were acquired in amplitude modulation mode, using a Si tip (Micromasch, k ~ 5 N/m, f = 160 KHz), an image resolution of 256 pixels per line, and at scan rate of 1 KHz.

FM-KPFM characterization. Local surface potential and capacitance (dielectric) measurements were acquired by frequency modulation (FM) 2-pass KPFM scanning, using a Pt/Ir coated tip (NT-MDT, k ~ 11.8 N/ m, f ~ 240 KHz). The image resolution was 256 pixels per line and the scan rate 0.7 KHz. FM-KPFM was selected because this mode is sensitive to the electrostatic force gradient (dF_{el}/dz) rather than the electrostatic force (F_{el}). This operation mode substantially decreases capacitive contributions from the tip beam or cantilever (C_b). Therefore, higher spatial and energy resolutions compared to amplitude modulation (AM) KPFM are usually obtained. During the first pass, the tip scans the surface in amplitude modulation mode at the tip's fundamental resonance frequency (ω) to trace the topography information. In the in second pass, the tip is lifted 10 nm from the surface, and a low frequency (ω_{ac} = 1 KHz) and amplitude (3 V) AC voltage is applied between the tip and the sample. While the tip retraces the surface, the sample's electrostatic force (F_{el}) and gradient (F_{el}/dz) are modulated by the AC bias. As a result of the F_{el} modulation, the side peaks ω_{mod} and $2\omega_{mod}$ emerge far below the fundamental frequency ω of the cantilever. Whereas the sidebands $\omega \pm \omega_{mod}$ and $\omega \pm 2\omega_{mod}$ arising adjacent to ω results from the F_{el}/dz modulation. A DC voltage is applied to nullify $\omega \pm \omega_{mod}$. This DC voltage is equal to the contact potential difference (CPD) value between the tip and the sample. Given that $F_{el} = -\frac{1\partial C}{2\partial z}(V_{DC} + V_{CPD})^2 - \frac{1\partial C}{4\partial z}V_{AC}^2$ and FM-KPFM follows dF_{el}/dz, it is possible to track simultaneously the second derivative of the capacitance $\partial^2 C/\partial z^2$ by the second harmonic of the digital lock-in in the KPFM electronic set-up.

TEPL characterization. TEPL experiments were acquired in a HORIBA NanoRaman HR Evolution, equipped with a 100x objective, and a 633 nm laser wavelength. A soft non-contact AFM Au tip (Omni-TERS probe, APP Nano, k ~5 N/m) was used as a TEPL probe. The laser power was around 0.2 mW and acquisition time 0.3 s per pixel. During imaging, the TEPL signal was acquired in contact mode while the lateral movement between pixels was performed in amplitude modulation. The raw hyperspectral map was corrected by subtracting the far-field signal from the near-field signal to acquire the final TEPL data.

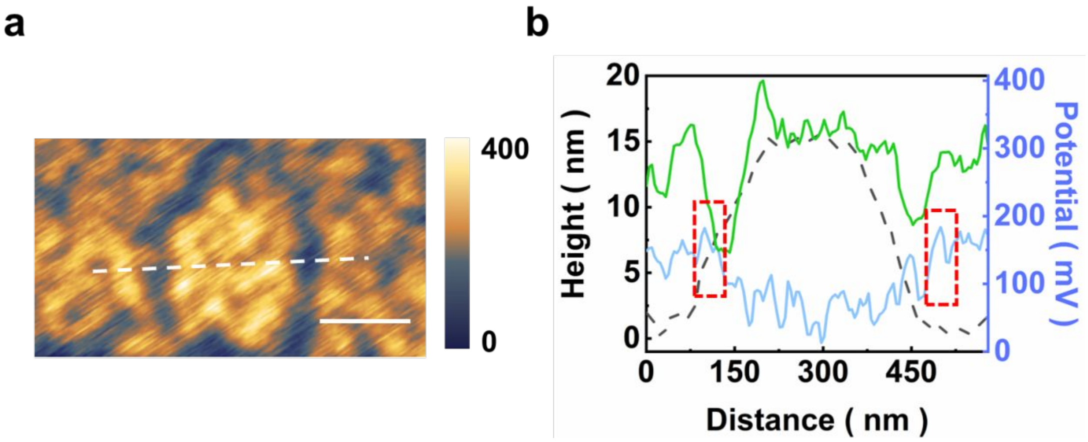

Figure S1. (a) KPFM measurements on monolayer WS_2 bubbles with illumination mentioned in Figure 1a. (b) Height profile, relative SP profile w/o and with illumination on monolayer WS_2 bubbles mentioned in Figure 1a along the white dashed line, corresponding to the black dashed line, the blue line and the green line, respectively. (a), scale bar, 200 nm.

On the monolayer WS_2 bubbles, we can also observe the SP sharp change at the edge of the bubble (red box region), as well as the SP enhancement on the bubbles area with illumination in accordance with the WS_2 bubbles on monolayer graphene. But unlike the WS_2 bubbles on monolayer graphene, due to the strong coupling between the monolayer WS_2 bubbles, the SP in the most of the WS_2 region elevates on illumination, no matter the bubble area or flat area.

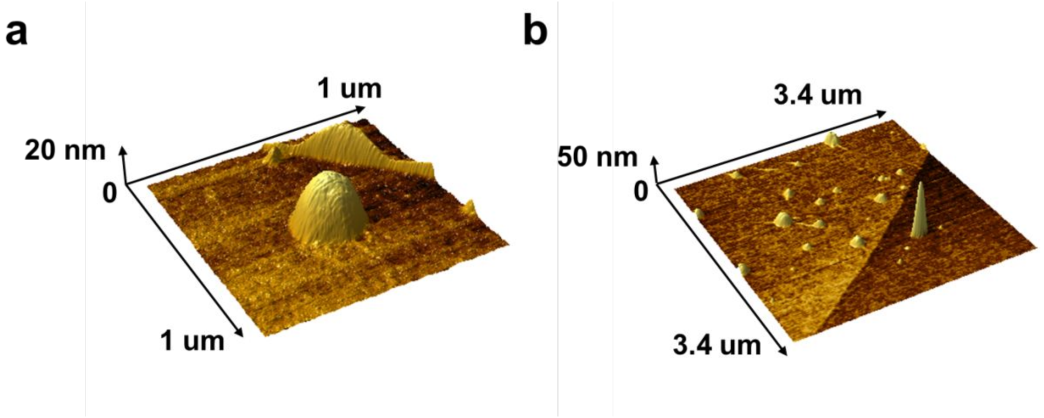

Figure S2. (a) Three-dimensional image of the large monolayer WS_2 bubble mentioned in Figure 2a. (b) Three-dimensional image of the pocket monolayer WS_2 bubble mentioned in Figure 2b.

In Figure S2, the morphologies of the bubbles are rendered stereoscopically, giving us a better understanding of the bubbles.

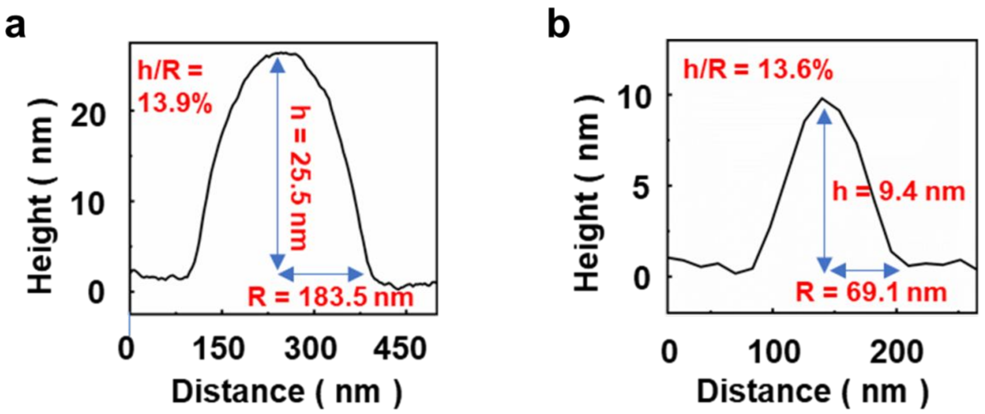

Figure S3. (a, b) Profile of the large bubble's and pocket bubble's height along the white dashed line in Figure 2a for (a) and in Figure 2b for (b).

The consistent *h/R* value of the large bubbles and pocket bubbles indicates similar strain distribution for different height bubbles.

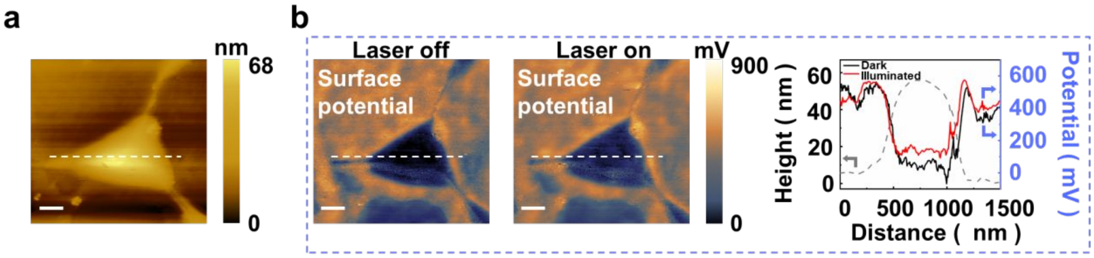

Figure S4. Comparison of surface potential variations w/o and with illumination of monolayer WS_2 bubbles on hBN. (a) AFM topography measurements of WS_2 bubbles on hBN. (b) Frequency modulation kelvin probe force microscopy (FM-KPFM) measurements of huge WS_2 bubbles on hBN (a) for (b). Profile of height, relative potential w/o and with illumination along the white dashed lines in (a), in the left and middle panels of (b), respectively. All scale bars, 200 nm. The pixel size is 5.84×5.84 nm^2.

In the left panel of Figure S4 b, high potential regions were still visible at the edge of WS_2/hBN nanobubbles w/o illumination, indicating the presence of a piezoelectric field. And in the right panel of Figure S4 b, the potential in the WS_2/hBN nanobubble region remained elevated with illumination, consistent with the observations in our WS_2/graphene system. This comparative experiment evades WS_2/graphene interlayer charge transfer influence for the intrinsic piezoelectric properties of WS_2 nanobubbles.

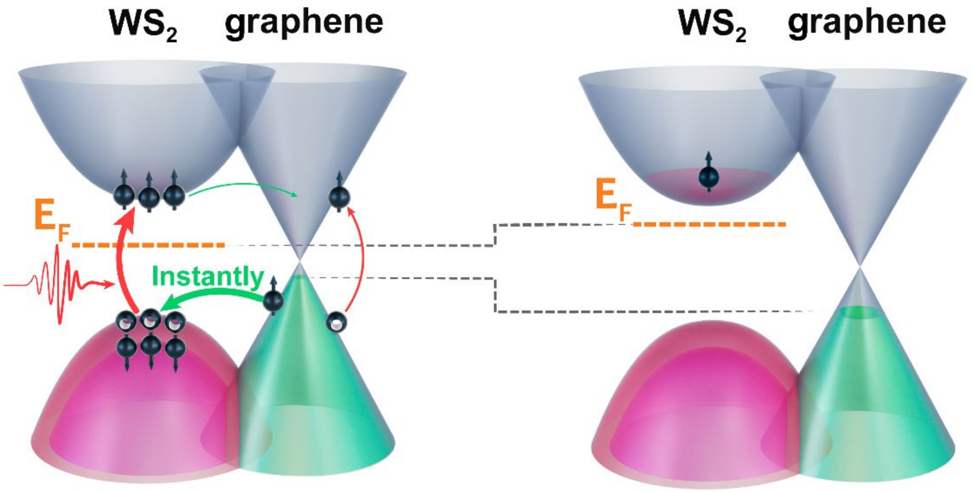

Figure S5. Schematic diagram of the charge transfer and the induced Fermi energy level shift of the vertical WS$_2$/graphene heterojunction with illumination.

The schematic diagram explicitly reveals the charge transfer process of WS$_2$/graphene heterojunction, electrons from graphene valence band recombine photogenerated holes of WS$_2$ layer, inciting the photoinduced electrons aggregation of WS$_2$ layer, interpreting SP reduction of WS$_2$ layer with illumination in monolayer WS$_2$/monolayer graphene heterostructure system.

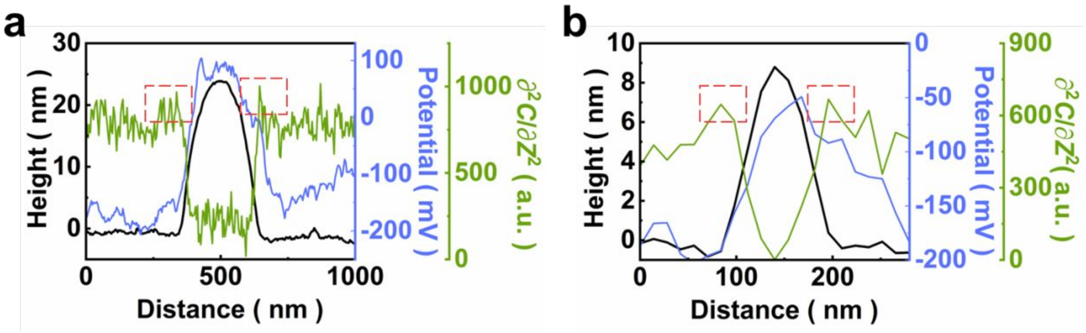

Figure S6. (a, b) Height, the total SP difference ΔV_{total} and $\partial^2 C/\partial z^2$ profile w/o illumination of the large monolayer WS$_2$ bubble in Figure 2a for (a) and of the pocket monolayer WS$_2$ bubble in Figure 2b for (b). The red squared sections are the high dielectric zones.

From Figure S6, an obvious difference of ΔV_{total} around the high dielectric regions is shown for the large bubbles and the distinguish becomes small for the pocket bubbles. But the tendency is the same for the large and the pocket bubbles. ΔV_{total} is more positive for the bubble area than the flat area.

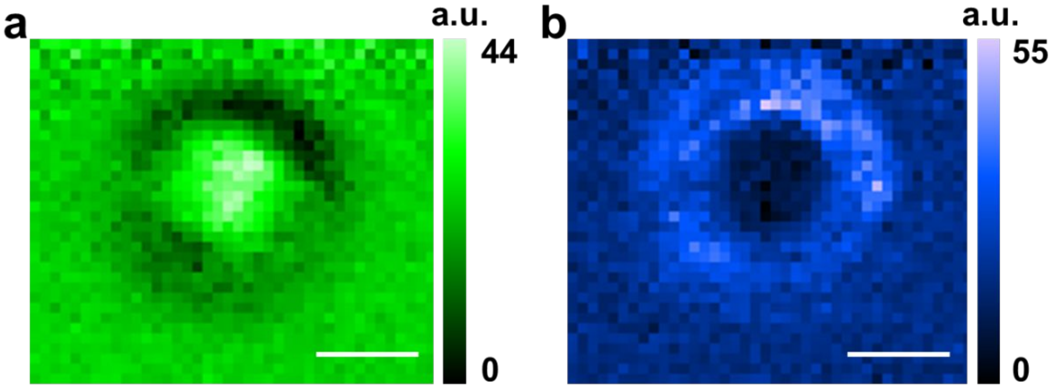

Figure S7. (a, b) Spatial mapping of the TEPL peak intensity of the large monolayer WS_2 bubble in Figure 2a ranging over the spectrum between 1.82 eV and 1.87 eV for (a), between 1.87 eV and 1.92 eV for (b), respectively. All scale bars, 100 nm.

We can discover an apparent red-shift of the TEPL peak position of the large monolayer WS_2 bubble in Figure 2a from the bubble edge to the bubble top through Figure S7.

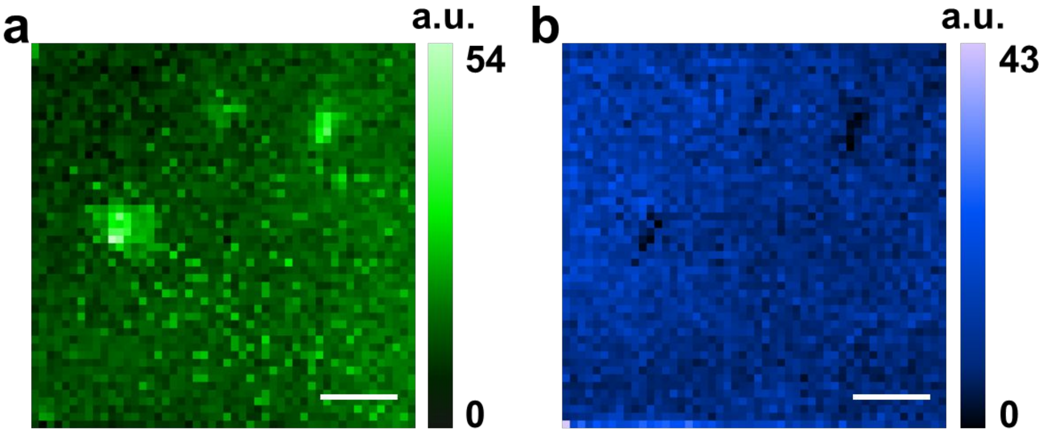

Figure S8. (a, b) Spatial mapping of the TEPL peak intensity of the pocket monolayer WS_2 bubble in Figure 2b ranging over the spectrum between 1.86 eV and 1.90 eV for (a), between 1.90 eV and 1.94 eV for (b), respectively. All scale bars, 200 nm.

We can also discover an apparent red-shift of the TEPL peak position the pocket monolayer WS_2 bubble in Figure 2b from the bubble edge to the bubble top through Figure S8.

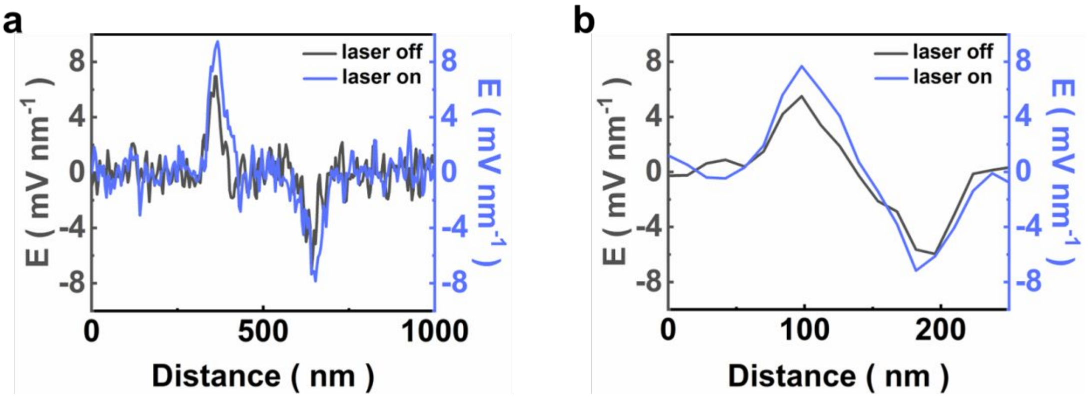

Figure S9. (a, b) Comparison of electrical field images w/o and with illumination of the large monolayer WS_2 bubble in Figure 2a for (a) and of the pocket monolayer WS_2 bubble in Figure 2b for (b).

From Figure S9a, an evident rise of the electrical field strength after illumination is observed on account of the opposite directional SP changes of the flat area and bubble area. From Figure S9b, a negligible increase can be discovered after illumination depending on the consistent directional SP changes of the flat area and bubble top area. The overall electrical field strength for the pocket bubble decreases compared with the large one.

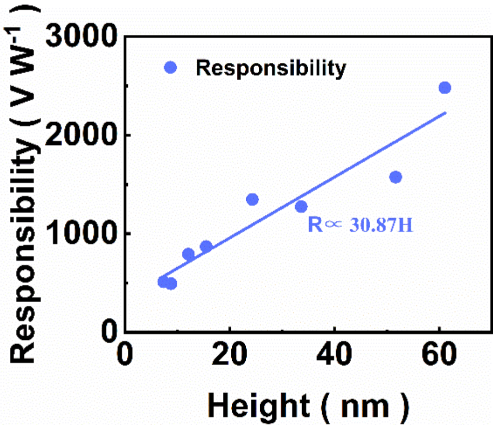

Figure S10. The relationship between the photoresponse of the bubbles with the bubble’s height.

Our input laser power is 0.2 mW. We divided this power value by the total SP difference ΔV_{total} to acquire the photoresponse. We can find the photoresponse enlarging almost linearly as the bubble’s height increases.

Supporting Note 1. Introduction of FM-KPFM mode

We choose two-pass FM-KPFM mode to acquire the topography, relative SP and $\frac{\partial^2 C}{\partial z^2}$ profiles of the WS_2 bubbles. Here are the widely known relations for the electrostatic force existed between the cantilever and the sample when applying a bias voltage at the DC voltage V_{DC} and frequency w_m amplitude V_{AC}:[1]

$$F_{DC} = -\frac{1}{2}\frac{\partial C}{\partial z}(V_{DC} + V_{CPD})^2 - \frac{1}{4}\frac{\partial C}{\partial z}V_{AC}^2$$

$$F_{w_m} = -\frac{\partial C}{\partial z}(V_{DC} + V_{CPD})V_{AC}sin(w_m t)$$

$$F_{2w_m} = \frac{1}{4}\frac{\partial C}{\partial z}V_{AC}^2 cos(2w_m t)$$

The derivatives of the components F_{w_m} and F_{2w_m} on Z-axis are two nonzero oscillations at frequencies w_m and $2w_m$. In accordance with the equation S2, FM-CPD can be acquired when F_{w_m} is zero ($V_{DC} + V_{CPD} = 0$). And DMag2 ($\frac{\partial^2 C}{\partial z^2}$) is proportional to the Z-derivative of F_{2w_m} (the equation S3) (the Kelvin feedback is opened), which reflects the local capacitance information of the sample.

From the capacitance model presented by Fumagalli, the capacitance can be depicted as:

$$C = 2\pi\varepsilon_0 R \ln\left(1 + \frac{R(1 - sin\theta_0)}{z + \frac{t}{\varepsilon}}\right)(S4)$$

Where $R,\ \theta_0,\ t,\ \varepsilon,\ z$ are the tip curvature, cone of the half angle of the tip, the film thickness, dielectric constant of the film and the tip-sample distance. The formula indicates that the DMag2 is approximately proportional to the permittivity.

Supporting Note 2. Calculation of the bubbles' strain distributions

We have referred to the method of strain calculation in this article. [2] To simplify the calculation, the Airy stress function η is constructed. We can acquire the function η through the AFM topography statistics,

$$\nabla^2\nabla^2\eta = -Y\left[\frac{\partial^2 h}{\partial x^2}\frac{\partial^2 h}{\partial \mathrm{y}^2} - \left(\frac{\partial^2 h}{\partial \mathrm{y}\partial \mathrm{x}}\right)^2\right](S5)$$

where Y, h are the Young's modulus (for monolayer WS_2, $Y=177\ \mathrm{N\ m^{-1}}$) and the height of the bubbles, respectively.

Via the Airy stress function η, we can compute the components of the stress tensor by the following three equations,

$$\sigma_{xx} = \frac{\partial^2\eta}{\partial \mathrm{y}^2}(S6)$$

$$\sigma_{xy} = -\frac{\partial^2\eta}{\partial y\partial x}(S7)$$

$$\sigma_{yy} = \frac{\partial^2\eta}{\partial x^2}(S8)$$

where σ_{ij} are the components of the stress tensor.

The stress-strain relationships can be expressed by Hooke's law,

$$\sigma_{\mathrm{xx}} = \frac{\mathrm{Y}}{1-v^2}(\epsilon_{xx} + v\epsilon_{yy})(S9)$$

$$\sigma_{xy} = \frac{Y}{1+v}\epsilon_{xy}(S10)$$

$$\sigma_{yy} = \frac{Y}{1-v^2}(\epsilon_{yy} + v\epsilon_{xx})(S11)$$

where $\epsilon_{\mathrm{ij}}, v$ are the components of the strain tensor and the Poisson ration of the material, respectively.

Finally, the strain of the bubbles can be obtained by

$$\epsilon = \epsilon_{\mathrm{xx}} + \epsilon_{\mathrm{yy}}(S12)$$

where ϵ is the strain of the bubbles.

Supporting Note 3. Calculation of piezoelectric coefficient

2H-WS_2 belongs to the D_{3h} point group, the symmetry conservation makes only one e-coefficient needed to be calculated. When a stress field is applied, e_{11} can be calculated by the subsequent formula, [3]

$$e_{11} = \frac{\partial \sigma_{11}}{\partial E_{11}} (S13)$$

where e_{11},σ_{11},E_{11} represent the piezoelectric coefficient, the stress and the piezoelectric field strength, respectively.

As shown in earlier work, the internal pressure of bubbles is just determined by the characteristics of the vdW heterostructure. This means the internal pressure is the common denominator if we confirm the material system. And our bubbles have regular internal pressure related to their sizes. The below equation is to calculate the pressure (P) inside the bubbles(when the strain $\epsilon \approx 0$), [4,5]

$$P = \frac{Y}{cvh}\left[4c_1\left(\frac{h}{R}\right)^4\right](S14)$$

where Y, h, R, ϵ are the Young's modulus (for WS_2, Y=177 N m^{-1}), the height, the radius and the strain of the bubbles, respectively. c_1,c_2,cv are some coefficients (when bending rigidity and strain are neglected $c_1 \approx 0.7, c_2 \approx 0.6, cv \approx 1.7$).

Then we calculate the stress utilizing the following formula roughly. We multiply the internal and external pressure difference by the membrane thickness to represent the stress. In this model, we assume the bubble region's stress is constant, [6]

$$\sigma = (P - P_0)t(S15)$$

where σ,P_0,t account for the stress, the pressure outside the bubbles, the thickness of monolayer WS_2.

The next step is to numerate the piezoelectric field. We divide the distance from the bubble top to the bubble edge by their SP difference, [6]

$$E = \frac{V_{edge} - V_{top}}{\sqrt{R^2 + h^2}} (S1.6)$$

where E,V_{edge},V_{top} are the strength of piezoelectric field, the surface potential of the bubble edge and top, respectively.

References

(1) Luo, Y.; Ding, X.; Chen, T.; Lin, G.; Su, T.; Chen, D. Imaging the Permittivity of Thin Film Materials by Using Scanning Capacitance Microscopy. *Appl. Sci.* **2022**, *12*, 11979.

(2) Darlington, T. P.; Krayev, A.; Venkatesh, V.; Saxena, R.; Kysar, J. W.; Borys, N. J.; Jariwala, D.; Schuck, P. J. Facile and Quantitative Estimation of Strain in Nanobubbles with Arbitrary Symmetry in 2D Semiconductors Verified Using Hyperspectral Nano-Optical Imaging. *J. Chem. Phys.* **2020**, *153*, 024702.

(3) Duerloo, K.-A. N.; Ong, M. T.; Reed, E. J. Intrinsic Piezoelectricity in Two-Dimensional Materials. *J. Phys. Chem. Lett.* **2012**, *3*, 2871-2876.

(4) Khestanova, E.; Guinea, F.; Fumagalli, L.; Geim, A.; Grigorieva, I. Universal Shape and Pressure inside Bubbles Appearing in Van Der Waals Heterostructures. *Nat. Commun.* **2016**, *7*, 12587.

(5) Dai, Z.; Hou, Y.; Sanchez, D. A.; Wang, G.; Brennan, C. J.; Zhang, Z.; Liu, L.; Lu, N. Interface-Governed Deformation of Nanobubbles and Nanotents Formed by Two-Dimensional Materials. *Phys. Rev. Lett.* **2018**, *121*, 266101.

(6) Wang, W.; Zhou, L.; Hu, S.; Novoselov, K. S.; Cao, Y. Visualizing Piezoelectricity on 2D Crystals Nanobubbles. *Adv. Funct. Mater.* **2021**, *31*, 2005053.